PHYSICAL REVIEW FLUIDS **5**, 094001 (2020)

Stability of gravity-driven liquid films overflowing microstructures with sharp corners

Henning Bonart,[*] Sangitha Rajes, Johannes Jung, and Jens-Uwe Repke[†]
Process Dynamics and Operations Group, Technische Universität Berlin, Straße des 17. Juni 135, 10623 Berlin, Germany

(Received 11 February 2020; accepted 17 August 2020; published 2 September 2020)

We report on the stability of thin liquid films overflowing single microstructures with sharp corners. The microstructures were of rectangular and triangular shape. Their heights and widths were 0.25, 0.5, and 0.75 times the Nusselt film thickness. To observe steady, wavy, and very unstable films we performed simulations with Reynolds numbers ranging from 10 to 70. The dynamics of the liquid film and the overflowing gas phase were described by the coupling between the Cahn-Hilliard and the Navier-Stokes equations. The resulting model forms a very tightly coupled and nonlinear system of equations. Therefore we carefully selected the solution strategy to enable efficient and accurate large-scale simulations. Our results showed that the formation of waves was shifted to higher Reynolds numbers compared to the film on a smooth surface. If waves were finally formed, the microstructures led to irregular waves. Our results indicate a great influence of the microstructure's shape and dimension on the stability of the overflowing liquid film.

DOI: 10.1103/PhysRevFluids.5.094001

I. INTRODUCTION

Gravity-driven liquid films overflowing a solid, structured surface appear in numerous technical applications. Examples include falling film evaporators and structured high-performance packing for absorption columns. The packing surfaces are often textured with microstructures with geometrical dimensions of the same order as the magnitude of the film thickness. To improve the performance of these textured packings and enable the design of new surfaces, knowledge about the stability of the overflowing thin liquid films is crucial. For research conducted on the stability of thin liquid films flowing on smooth and flat substrates including wave phenomena we refer to the review by Craster and Matar [1] and the summary in the recent review by Aksel and Schörner [2, chap. 5.1].

The influence of undulated periodic wavy surfaces on the stability of the film has been experimentally and numerically studied by a lot of groups. Wierschem *et al.* [3] showed that long-wave bottom undulations stabilize the flow. For sufficiently short wavelengths of the topography D'Alessio *et al.* [4] found that the fluid gets destabilized. Trifonov [5] found that the stability strongly depends on both the surface topography and the physical properties of the liquid. The complexity of the stability of liquid films was again recently illustrated by Schörner *et al.* [6].

Periodical rectangular corrugations were studied experimentally and numerically by Argyriadi *et al.* [7] and Pak and Hu [8], respectively. They found that the structures deformed the shape of the liquid film. The strong influence of the amplitude of rectangular corrugations on the stability of the

[*]henning.bonart@tu-berlin.de
[†]jens-uwe.repke@tu-berlin.de; www.dbta.tu-berlin.de

liquid film was reported by Tseluiko *et al.* [9]. Schörner *et al.* [10] concluded that the specific bottom shape does not have a strong influence on the stability for a wide range of flows and geometries.

In contrast, for single-phase flows it is well known that sharp corners have a great influence on stability and flow separation (see, for example, [11–14]). Surprisingly, to the best of our knowledge, only a few papers discuss the results on thin liquid films and single microstructures with sharp corners and a positive increase in the size of the film itself. As stated by Veremieiev *et al.* [15], the simulation of perfectly steep sides without any smoothing is not possible with simpler models but requires the numerical solution of the Navier-Stokes (NS) equations. Some results were documented on the influence of smooth localized microstructures, like hemispheres [15,16], on the stability of liquid films. Results on trenches or single step-ups or -downs with sharp corners were described by Veremieiev *et al.* [15,17] and Gaskell *et al.* [18]. However, despite their relevance in technical applications, systematic studies of the influence of separated, sharp structures on the stability of the film are rarely found.

In this paper we report on detailed numerical simulations of films overflowing separated microstructures with sharp corners. The dynamics of the two-phase flow are described by the coupling between the Cahn-Hilliard (CH) and the Navier-Stokes equations. In this way, we are able to fully resolve the sharp corners. The resulting model forms a very tightly coupled and nonlinear system of equations. Therefore we carefully select the solution strategy to enable efficient and accurate simulations. This includes the linearization and decoupling of the equations and preconditioned Krylov methods for the solution of the arising linear systems. The examined microstructures are of rectangular and triangular shape with heights and widths of 0.25, 0.5, and 0.75 compared to the particular Nusselt film thickness. The Reynolds numbers range from 10 to 70.

The remainder of the article is structured as follows: In Sec. II, we discuss the governing equations and present the system in nondimensional form. The numerical method is described in Sec. III. There, we give details on the decoupling of the equations, the descretization, and the preconditioner. The test case is described in Sec. IV. Finally, we present and discuss our results in Sec. V. In Sec. VI we conclude our paper.

II. CAHN-HILLIARD–NAVIER-STOKES (CHNS) EQUATIONS

We treated the liquid film as well as the overflowing gas phase as Newtonian, isothermal, immiscible, and incompressible fluids. The thermodynamically consistent CHNS model presented in [19] was applied. The model combines the common incompressible, single-field NS equations with the convective CH equations to describe the interface dynamics between the liquid and the gas. It is given by

$$\rho\partial_t \boldsymbol{v} + ((\rho\boldsymbol{v} + \boldsymbol{J})\cdot\nabla)\boldsymbol{v} - \operatorname{div}(2\eta D\boldsymbol{v}) + \nabla p = -\varphi\nabla\mu + \rho\boldsymbol{g}, \tag{1}$$

$$-\operatorname{div}(\boldsymbol{v}) = 0, \tag{2}$$

$$\partial_t\varphi + \boldsymbol{v}\cdot\nabla\varphi - b\Delta\mu = 0, \tag{3}$$

$$-\sigma\epsilon\Delta\varphi + \frac{\sigma}{\epsilon}W'(\varphi) = \mu, \tag{4}$$

and the boundary conditions

$$\boldsymbol{v}^{\text{plate}} = \boldsymbol{0}, \tag{5}$$

$$v_y^{\text{top}} = 0, \tag{6}$$

$$\boldsymbol{v}^{\text{inlet}} = \boldsymbol{v}^{\text{outlet}}, \tag{7}$$

$$\nabla_y\varphi = \nabla_y\mu = 0, \tag{8}$$

with the velocity field $\boldsymbol{v}$, the pressure field p, the phase field φ, and the chemical potential μ. The velocity deformation tensor and the gravitational acceleration are given by $D\boldsymbol{v} := \frac{1}{2}(\nabla\boldsymbol{v} + (\nabla\boldsymbol{v})^t)$

and $\boldsymbol{g}$. The density function is denoted $\rho(\varphi)$ and satisfies $\rho(-1) = \rho_1$ and $\rho(1) = \rho_2$, with $\rho_2 > \rho_1 > 0$ denoting the constant densities of the two involved fluids. The viscosity function is $\eta(\varphi)$ and satisfies $\eta(-1) = \eta_1$ and $\eta(1) = \eta_2$, with η_1, η_2 denoting the viscosities of the involved fluids. For this work, they were chosen as:

$$\rho = \frac{1}{2}((\rho_l + \rho_g) + \varphi(\rho_l - \rho_g)), \quad \eta = \frac{1}{2}((\eta_l + \eta_g) + \varphi(\eta_l - \eta_g)). \tag{9}$$

Equations 1 and 2 are the common incompressible NS equations with two additional terms: The density flux $\boldsymbol{J} := -b\frac{\partial\rho}{\partial\varphi}\nabla\mu$ guarantees consistency and enhances stability if the densities of the two fluids are different. The surface tension force is modeled by $\varphi\nabla\mu$. The parameter b stems from the diffuse interface approach in the CH equations, (3) and (4). It represents the mobility of the two-phase interface. The thickness of the diffuse interface is described by ϵ. The scaled surface tension is given by $\sigma = \frac{3}{2\sqrt{2}}\sigma^{\text{phy}}$ with the physical surface tension σ^{phy}. The function $W(\varphi)$ denotes a dimensionless potential of double-well type with two strict minima at ± 1. Here, we chose it as

$$W(\varphi) := \begin{cases} \frac{1}{4}(1-\varphi^2)^2 & \text{if} \quad |\varphi| \leqslant 1, \\ (|\varphi|-1)^2 & \text{otherwise.} \end{cases} \tag{10}$$

For different choices of W and a comparison we refer to [20].

The model, (1) and (2), can be derived purely from thermodynamic principles [19]. It is postulated that the system in the whole domain Ω can be described by the following sum of the kinetic energy and Helmholtz free energy functional of the Ginzburg-Landau type [21]:

$$E = \frac{1}{2}\int_\Omega \rho|\boldsymbol{v}|^2\, dx + \sigma\int_\Omega \epsilon^{-1}W(\varphi) + \epsilon|\nabla\varphi|^2\, dx. \tag{11}$$

Compared to sharp interface methods, the phase-field method replaces the infinitely thin boundary between gas and liquid by a transition region of finite thickness. It describes the distribution of the different fluids by a smooth indicator function where -1 is pure gas and $+1$ is pure liquid. It follows that all physical properties like density and viscosity vary continuously across the interface. As summarized in the review by Wörner [22], the CHNS equations can easily handle large topological changes of the interface [23] and the interface is implicitly tracked without any prior knowledge of the position. Furthermore, one of the major advantages is that the formulation of the surface tension force in the NS equation conserves both the surface tension energy and the kinetic energy. This can reduce spurious currents, which are purely artificial velocities around the interface, to the level of the truncation error even for low capillary numbers [24,25].

A. Nondimensionalization

We scale the coupled CHNS system, Eqs. (1) to (4), with

$$t = \frac{\hat{t}L}{U}, \quad x = L\hat{x}, \quad \boldsymbol{v} = U\hat{\boldsymbol{v}}, \quad p = U^2\rho_l\hat{p}, \quad \mu = \frac{U\eta_l}{L}\hat{\mu},$$
$$\rho = \hat{\rho}(\rho_l + \rho_g), \quad \eta = \hat{\eta}(\eta_l + \eta_l), \quad \boldsymbol{g} = \frac{U^2}{L}\hat{\boldsymbol{g}} \tag{12}$$

and apply the following nondimensional groups:

$$\text{Re} = \frac{\rho_l UL}{\eta_l}, \quad \text{Ca} = \frac{\eta_l U}{\sigma}, \quad A_\rho = \frac{\rho_l - \rho_g}{\rho_l + \rho_g}, \quad A_\eta = \frac{\eta_l - \eta_g}{\eta_l + \eta_g}, \quad \text{Cn} = \frac{\epsilon}{L}, \quad \text{Pe}_\epsilon = \frac{\epsilon LU}{b\sigma}, \tag{13}$$

where $L = \delta_{\mathrm{nu}}$ and $U = \bar{v}_{\mathrm{nu}}$ are the Nusselt film height and the mean film velocity, respectively. Both are calculated for a specific Reynolds number Re and the inclination angle α measured from the plate to the horizontal with

$$\delta_{\mathrm{nu}} = \sqrt[3]{\frac{3\eta_l^2 \mathrm{Re}}{\rho_l^2 g_x \sin\alpha}}, \tag{14}$$

$$\bar{v}_{\mathrm{nu}} = \frac{\delta_{\mathrm{nu}}^2 \rho_l g_x \sin\alpha}{3\eta_l}. \tag{15}$$

In this way the physical system is characterized by the

(i) Reynolds number Re (inertial over viscous forces in the film),

(ii) Capillary number Ca (viscous drag in the film over surface tension forces between film and gas), and

(iii) Atwood numbers A_ρ and A_η (density and viscosity ratios between film and gas).

The Cahn number Cn and the Peclet number Pe_ϵ stem from the CH approach and describe the dynamics of the diffuse interface.

We obtain the following nondimensionalized CHNS system:

$$\rho\partial_t \boldsymbol{v} + ((\rho\boldsymbol{v} + \boldsymbol{J})\cdot\nabla)\boldsymbol{v} - \mathrm{Re}^{-1}\mathrm{div}(2\eta D\boldsymbol{v}) + \nabla p = -\mathrm{Re}^{-1}\varphi\nabla\mu + \mathrm{Ca}^{-1}\mathrm{Re}^{-1}\rho\boldsymbol{g}, \tag{16}$$

$$-\mathrm{div}(\boldsymbol{v}) = 0, \tag{17}$$

$$\partial_t\varphi + \boldsymbol{v}\cdot\nabla\varphi - \mathrm{CaCnPe}_\epsilon^{-1}\Delta\mu = 0, \tag{18}$$

$$-\mathrm{Cn}^2\Delta\varphi + W'(\varphi) = \mathrm{CaCn}\mu, \tag{19}$$

with $J := -\mathrm{CaCnPe}_\epsilon^{-1}\frac{\partial\rho}{\partial\varphi}\nabla\mu$ and

$$\rho = \frac{1}{2}(1 + \varphi A_\rho)), \quad \eta = \frac{1}{2}(1 + \varphi A_\eta)). \tag{20}$$

For better readability we have omitted the hat above all scaled variables and operators. If not otherwise noted, beginning with Eq. (16) all variables are scaled and dimensionless.

III. NUMERICAL METHOD

A. Discretization

For a practical implementation in a finite-element scheme a time grid $0 = t_0 < t_1 < \ldots < t_{m-1} < t_m < \ldots < t_M = T$ on $I = [0, T]$ with a nonequidistant time step size $t_m - t_{m-1} = \tau^m > 0$ for $m = 1, \ldots, M$ is introduced. Further, a triangulation $\mathcal{T}_h$ of the domain into cells T_i is introduced such that $\mathcal{T}_h = \bigcup_{i=1}^N T_i$ covers the domain. The specific meshing is discussed in Sec. IV. On $\mathcal{T}_h$ we introduced piecewise linear Lagrange finite elements $V_1 = \mathcal{P}_1$ for φ_h, μ_h, and p_h and the triangular/tetrahedral Mini element $V_M = \mathcal{P}_1 \bigoplus \mathcal{B}_{1+d}$, denoting the space of linear polynomials enriched by a cubic bubble function, for $\boldsymbol{v}_h$. For the derivation of the weak form as well as the proof of energy stability and thermodynamic consistency we refer to [20]. Note that we omit the notation of vectors as bold symbols for better readability henceforth.

Given $\varphi^{m-1} \in V_1$, $\mu^{m-1} \in V_1$, and $\boldsymbol{v}^{m-1} \in V_M$, find $\varphi_h^m \in V_1$, $\mu_h^m \in V_1$, $p_h^m \in V_1$, and $\boldsymbol{v}_h^m \in V_M$, such that for all $\boldsymbol{w} \in V_M$, $q \in V_1$, $\Phi \in V_1$, and $\Psi \in V_1$ the following equations hold:

$$\begin{aligned}&\frac{1}{\tau^m}\left(\frac{\rho^m + \rho^{m-1}}{2}\boldsymbol{v}_h^m - \rho^{m-1}\boldsymbol{v}^{m-1}, \boldsymbol{w}\right)\\ &\quad + a(\rho^{m-1}\boldsymbol{v}^{m-1} + \boldsymbol{J}^{m-1}, \boldsymbol{v}_h^m, \boldsymbol{w}) + \left(\mathrm{Re}^{-1}2\eta^{m-1}D\boldsymbol{v}_h^m, D\boldsymbol{w}\right) - \left(\mathrm{div}\boldsymbol{w}, p_h^m\right)\\ &\quad + \left(\mathrm{Re}^{-1}\varphi^{m-1}\nabla\mu_h^m, w\right) - \mathrm{Ca}^{-1}\mathrm{Re}^{-1}(\boldsymbol{g}\rho^{m-1}, \boldsymbol{w}) = 0,\end{aligned} \tag{21}$$

$$-\left(\operatorname{div}\boldsymbol{v}_h^m, q\right) = 0, \tag{22}$$

$$\frac{1}{\tau^m}\left(\varphi_h^m - \varphi^{m-1}, \Psi\right) - \left(\varphi^{m-1}\boldsymbol{v}^{m-1}, \nabla\Psi\right) + \left(\mathrm{Re}^{-1}\frac{\tau^m|\varphi^{m-1}|^2}{\rho^{m-1}}\nabla\mu_h^m, \nabla\Psi\right)$$
$$+ \left(\mathrm{CaCnPe}_\epsilon^{-1}\nabla\mu_h^m, \nabla\Psi\right) = 0, \tag{23}$$

$$\left(\mathrm{Cn}^2\nabla\varphi_h^m, \nabla\Phi\right) + \left(W'(\varphi^{m-1}) + S_W(\varphi_h^m - \varphi^{m-1}), \Phi\right) - \left(\mathrm{CaCn}\mu_h^m, \Phi\right) = 0, \tag{24}$$

with $\boldsymbol{J}^{m-1} := -\mathrm{Pe}_\epsilon^{-1}\frac{\partial\rho}{\partial\varphi}(\varphi^{m-1})\nabla\mu^{m-1}$, $\rho^{m-1} := \rho(\varphi^{m-1})$, and $\eta^{m-1} := \eta(\varphi^{m-1})$. We decoupled the NS equation and the CH equation by using an augmented velocity field in Eq. (23) (see [26] and [27]). In this way, one can first solve Eqs. (23) and (24) and thereafter Eqs. (21) and (22). Furthermore, for W' a stabilized linear scheme was applied, where S_W is a suitable stabilization parameter. Note that this decoupled and linearized scheme is also energy stable and thermodynamically consistent (see [20] and [28]).

To control the time step size we used a simple and straightforward strategy. After every time step iteration we calculated the minimal time step based on two distinct Courant numbers, Co_v and Co_φ. The minimal time step τ_v^m was calculated following the well-known Courant relation (see [29]). Furthermore, to include the movement of the interface into the time step consideration, we followed [30] and replaced the velocity $\boldsymbol{v}^{m-1}$ with the phase-field velocity

$$\frac{\partial_t\varphi}{|\nabla\varphi|} \approx \frac{\varphi^{m-1} - \varphi^{m-2}}{\tau^{m-1}|\nabla\varphi^{m-1}|} \tag{25}$$

to obtain τ_φ^m. The next time step τ^m was chosen as the minimum of τ_v^m and τ_φ^m as well as $\tau_{\max} = 1e-4$ to restrict the time step size to reasonable values, especially at the beginning of the simulations:

$$\tau^m = \min\left(\min\left(\tau_v^m\right), \min\left(\tau_\varphi^m\right)s\right), \tau_{\max}) = \min\left(\min\left(\frac{\mathrm{Co}_v h}{|\boldsymbol{v}^{m-1}|}\right), \max\left(\frac{\mathrm{Co}_\varphi\tau^{m-2}h|\nabla\varphi^{m-1}|}{|\varphi^{m-1} - \varphi^{m-2}|}\right), \tau_{\max}\right). \tag{26}$$

B. Solver

We implemented the solution scheme given in Sec. III A in Python3 using the finite-element library FEniCS 2019.1.0 [31,32]. For the solution of the arising linear systems and subsystems the software suite PETSc 3.8.4 [33–35] was applied. At each time step we first solved the CH system and thereafter the NS systems. The CH system was solved using the direct linear solver MUMPS 5.1.1 [36,37]. Note that the naive usage of a Krylov method for unsymmetric systems, e.g., GMRES, preconditioned by a simple Gauss-Seidel or successive over relaxation method to solve the CH system results in a lot of outer iterations. We refer to [38] and [39] for efficient preconditioners for the CH system.

For the NS system we had to solve at every time step a linear system with the linear operator G:

$$G_{\mathrm{NS}} = \begin{pmatrix} \frac{1}{\tau}\left(\frac{\rho^m+\rho^{m-1}}{2}\boldsymbol{v}_h^m, \boldsymbol{w}\right) + a\left(\rho^{m-1}\boldsymbol{v}^{m-1} + \boldsymbol{J}^{m-1}, \boldsymbol{v}_h^m, \boldsymbol{w}\right) + \left(\mathrm{Re}^{-1}2\eta^{m-1}D\boldsymbol{v}_h^m, D\boldsymbol{w}\right) & -\left(\operatorname{div}\boldsymbol{w}, p_h^m\right) \\ -\left(\operatorname{div}\boldsymbol{v}_h^m, q\right) & 0 \end{pmatrix}$$
$$= \begin{pmatrix} A & B^T \\ B & 0 \end{pmatrix}. \tag{27}$$

Solving this large-scale saddle-point system is computationally very expensive. Furthermore, large meshes forbid the usage of direct linear solvers. Therefore, we applied PETSc's GMRES method preconditioned from the right. As preconditioner an upper triangular block preconditioner for

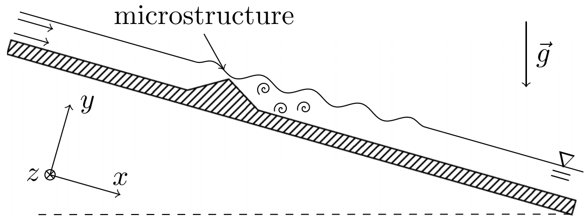

FIG. 1. Illustration of the simulation domain. Exemplarily, a triangular microstructure with a sharp corner is displayed.

Oseen-type problems was used:

$$P_{\mathrm{NS}} = \begin{pmatrix} \hat{A} & B^T \\ 0 & -\hat{S} \end{pmatrix}. \tag{28}$$

Here, S is an approximation of the Schur complement given by the pressure-convection-diffusion preconditioner

$$S^{-1} = R_p^{-1} + M_p^{-1}\big(I + K_p A_p^{-1}\big). \tag{29}$$

For details about this preconditioner we refer to [40–42]. Recently, this preconditioner was generalized to two-phase flows [43]. In this work, we used the following expressions for the matrices occurring in Eq. (29):

$$M_p = \frac{\mathrm{Re}}{\eta^{m-1}}\big(p_h^m, q\big), \tag{30}$$

$$K_p = \frac{\mathrm{Re}}{\eta^{m-1}} a\big(\rho^{m-1}\boldsymbol{v}^{m-1} + \boldsymbol{J}^{m-1}, p_h^m, q\big), \tag{31}$$

$$A_p = (\nabla p, \nabla q), \tag{32}$$

$$R_p = B(\mathrm{diag}(M_v))^{-1}B^T, \tag{33}$$

$$M_v = \frac{1}{\tau}\left(\frac{\rho^m + \rho^{m-1}}{2}\boldsymbol{v}_h^m, w\right), \tag{34}$$

where M_p and M_v are scaled pressure and velocity mass matrices, respectively, K_p is a scaled pressure convection matrix, and A_p is the pressure Laplacian.

For details on the implementation of the preconditioner we refer to the documentation of FENaPACK (https://fenapack.readthedocs.io). Besides the default options in FENaPACK and PETSc the Richardson method was applied together with an algebraic multigrid provided by Hypre as preconditioner for the inversion of A, R_p, and A_p. For the inversion of M_p the preconditioned Chebyshev iterative method together with a Jacobi preconditioner was used.

The model and the solution scheme as well as our implementation has been extensively validated. We obtained accurate results against the well-known rising bubble benchmark of Hysing *et al.* [44] (see [20]). Flows involving moving contact lines were validated against analytical solutions of spreading and pinned droplets in [45]. Again, we accomplished a very good agreement. We obtained an almost-perfect accordance with the analytical Nusselt film solution in [46]. For a validation involving film flows over corrugations, we matched our results with the experiments reported in [47] and the simulations in [48] (see Appendix A).

IV. SIMULATION CASE AND MESH

In Fig. 1 the simulation domain is illustrated. Exemplarily, a triangular obstacle with a base length and height of $h = 0.75$ is shown. Due to the nondimensionalization (see Sec. II A), h is

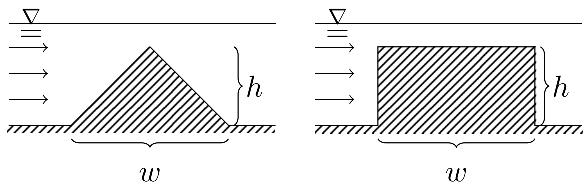

FIG. 2. Illustration of the microstructures.

always given relative to the film height. The geometries of the two examined microstructures are depicted in Fig. 2. We chose triangular and rectangular as representative structures, as they are the simplest forms with sharp corners. The solid surface was tilted to the horizontal at an angle α. The flow entered the simulation domain from the left and emitted at the right. The flow was purely driven by gravity with the gravitational acceleration constant g. On the bottom wall and the top opening no-slip and infinite-slip boundary conditions, respectively, were used (see Sec. II). To avoid the negative influence of in- and outflow boundary conditions, we applied periodic boundary conditions on the left and right sides of the domain. To reduce the computational effort, the size of the symmetric domain was $8L \times 4L$. Note that due to the periodic domain, we never simulated a single structure but periodic arrays of structures. However, we verified our assumption by comparing the shape of the interfaces for two different domain lengths (see Appendix B). We found that a distance of $7L$ between the simulated microstructure and the subsequent microstructure already is sufficient to approach a single structure. Note, however, that due to the periodicity, we might be missing some instability modes.

Figure 3 displays the mesh used in the simulations. The two-dimensional, unstructured, triangular, periodic meshes were generated using Gmsh [49]. The background cell diameter was of size $h_{\text{outer}} = 32\ \text{Cn}/5$. The area around the interface was resolved with $h_{\text{interface}} = 4\ \text{Cn}/5$, which resulted in around five cells over the interfacial thickness. It was found in [50] that this is sufficient to accurately capture the dynamics of the interface. The film was resolved with $h_{\text{film}} = 2h_{\text{interface}}$. In this way, the mesh consisted of 1594 vertices and 3075 elements. Using the scheme from Sec. III A and $\text{Cn} = 0.04$ the meshing resulted in around 16 000 and 55 000 degrees of freedom for the CH and the NS systems, respectively.

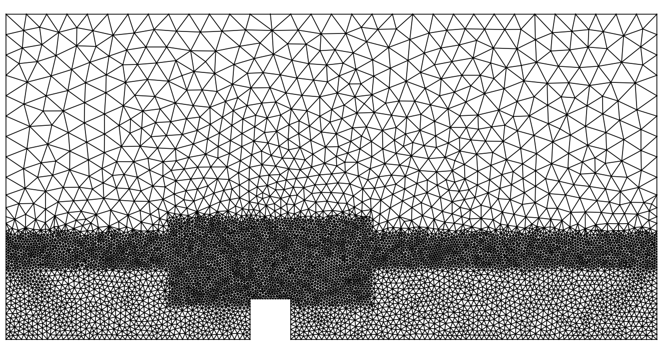

FIG. 3. Two-dimensional, unstructured, periodic, triangular mesh used in the simulations of the rectangular microstructures. It has three refinement zones: interface, film, and obstacle. The size of the bounding box is $8L \times 4L$. This mesh consists of around 1594 vertices and 3075 elements.

TABLE I. Nondimensional parameters used in the film flow simulations. For comparison, the corresponding Nusselt film thicknesses for an air and Basildon-BC10cs silicon oil system with $\sigma_{gl} = 18.87$ mN m^{-1}, $\rho_l = 924.3$ kg m^{-3}, $\rho_l = 924.3$ kg m^{-3}, $\eta_l = 10.721\,88$ mPa s, $\rho_g = 1.2$ kg m^{-1}, and $\eta_g = 0.018$ mPa s are displayed.

Re	Ca	A	A_η	Cn	Pe_ϵ	δ_{nu} (mm)
10	0.04				107	1.44
20	0.07				169	1.81
30	0.09				222	2.07
40	0.11	0.99	0.99	0.04	269	2.28
50	0.13				313	2.45
60	0.15				353	2.61
70	0.16				391	2.75

V. FILM FLOW OVER MICROSTRUCTURES

A. Setup

To compare the stability of the liquid films, we performed simulations with Reynolds numbers Re between 10 and 70. Following [48] we assume that two-dimensional structures can be represented with infinite depth normal to the main flow direction in a two-dimensional simulation. We initialized the simulation for a specific value of Re with a smooth film of height δ_{nu} calculated from Eq. (14). The remaining nondimensional parameters were calculated from the corresponding Re and Nusselt film quantities and truncated (see Table I). Due to the scaling of the simulation domain, the Cahn number Cn remained constant. The initial velocity of the film and the overflowing gas phase was 0, i.e., the liquid film as well as the gas phase was at rest. This corresponds to an initial inclination angle $\alpha = 0^\circ$. At the very beginning of the simulation the plate was flipped to an inclination of $\alpha = 8^\circ$. The simulations were performed until a final time of $T = 2$ s or until a steady state was reached. In Appendix B we verify that this final time is sufficient to approximate time-periodic results.

To decide if a steady state was reached, we looked at the change in the key variables, velocity v and phase field φ, over one time step [30]:

$$\Delta_v = \int_\Omega \frac{\left|v_x^m - v_x^{m-1}\right|}{\tau^m} dx, \quad \Delta_\varphi = \int_\Omega \frac{\left|\varphi^m - \varphi^{m-1}\right|}{\tau^m} dx. \tag{35}$$

Exemplarily, in Fig. 4 the steady-state criteria for two rectangular structures with $h = 0.75$ and $h = 0.5$ are plotted over time (left). Furthermore, we show the corresponding amplitude spectra measured at $x = 3$ for 1 to 2 s. It is clearly evident that the large rectangular microstructure with $h = 0.75$ led to very small changes from one time step to another in the first 0.5 s (gray lines). The steady state was reached very quickly, no waves were formed and the corresponding amplitude spectrum (bottom-right panel in Fig. 4) is 0. In contrast, the waves for $h = 0.5$ and Re = 70 completely prevented a steady state (black lines in Fig. 4).

B. Results

We observed a completely steady film for low Re and an onset of waves for intermediate Re. For larger Re we even saw a highly distorted film with irregular waves (see below or Figs. 5 and 6). In our case, the critical Reynolds number for a flat surface is calculated as $\mathrm{Re}_c = 5/4 \cot 8^\circ \approx 8.8$. Note that we did not apply any forced perturbations to the film flow, i.e., all instabilities occurred naturally. Therefore, we decided qualitatively that a film was unstable if any waves at all were formed after at most 2 s. Even in the flat-surface case we would therefore expect the formation of instabilities for longer time spans. A second criterion is that the amplitude spectrum is low without

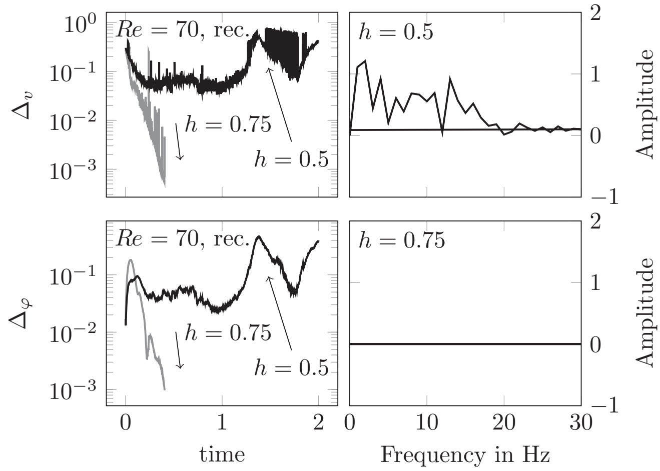

FIG. 4. Development of the steady-state criteria and the corresponding amplitude spectra at $x = 3$ for 1 to 2 s.

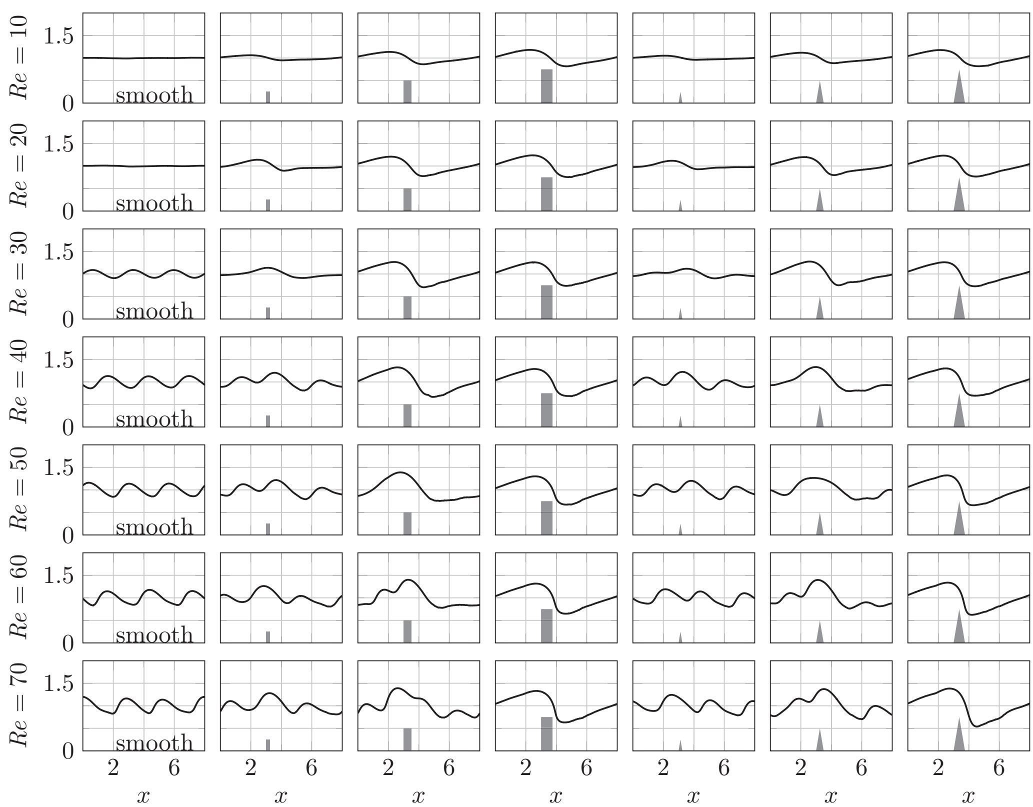

FIG. 5. Shape of the liquid film interface at $t = 2$ s for different values of Re. The domain is compressed and cut off at a height of 2.0. All dimensions are normalized with the respective film thickness δ.

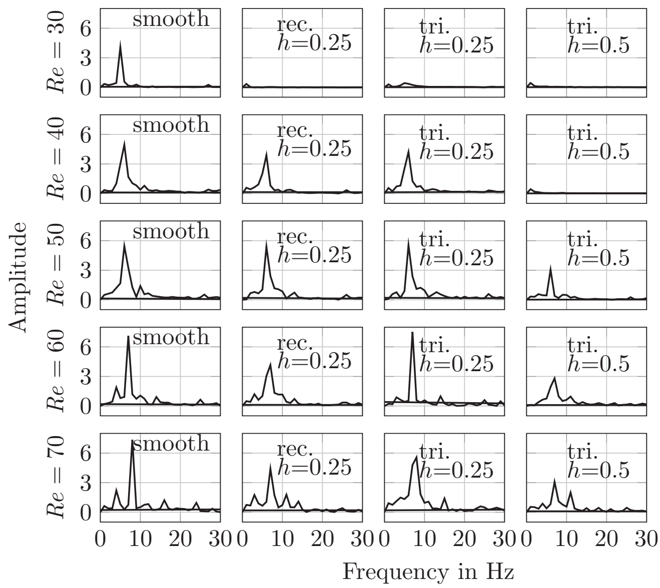

FIG. 6. Amplitude spectra for some liquid films calculated using a discrete Fourier transformation (DFT). Stable films with zero-amplitude spectra are omitted. The data for the DFT were extracted from the isolines (see Fig. 5) at $x = 3$ (right before the microstructures) for 1 to 2 s.

any pronounced peaks. In this way, we do not take a single, stagnant bump due to retention as a sign of an unstable film (for example, we consider the films in the fourth column in Fig. 5 stable).

In Fig. 5 the film surface obtained for two microstructures (rectangular and triangular) with height and width $h = w = 0.75\delta$, $h = w = 0.5\delta$, and $h = w = 0.25\delta$ are displayed for Reynolds numbers Re ranging from 10 to 70. For comparison the film over a smooth surface is shown in the first column. The film surfaces (depicted as solid black lines) were extracted from the simulation data as the isolines where $\varphi = 0$. The microstructures are illustrated as gray insets in Fig. 5. To gain more insight into the waves Fig. 6 shows amplitude spectra for a choice of configurations. The amplitudes were calculated using a discrete Fourier transformation. The data for the transformation were extracted from the isolines (see Fig. 5) at $x = 3$ (right before the microstructures) for 1 to 2 s.

The film over the smooth surface did not show any deformation for low Re values. Waves started to form at $\mathrm{Re} \geqslant 30$ and got more and more pronounced with increasing Re. However, even at $\mathrm{Re} = 70$, the waves stayed regular with a narrow frequency range. The amplitude spectra showed a pronounced, sharp peak for all Re values, which is a strong sign of regular waves.

We observed that all microstructures retained the film flow and greatly altered the film surface even for low Reynolds numbers. However, this retention before the microstructures led to a single, large hump or ridge already observed, for example, in [9], [16], and [51]. Compared to the film on the smooth plate, all three rectangular structures inhibited the formation of waves. This is apparent from the first row in Fig. 6, where all the amplitudes are almost 0 except for a sharp peak obtained for the smooth surface. The onset of the formation of waves was shifted to higher Reynolds numbers. Furthermore, we observed that the larger the structure compared to the film thickness, the stronger the inhibition (for example, compare columns 1 and 3 in Fig. 5). This was already observed in [6] for higher Reynolds numbers. Finally, if waves were formed for a critical Re, the waves were much more irregular than in the smooth case (compare, for example, rows 5 and 6, column 3, in Fig. 5). The dynamics of the waves can be observed in Fig. 7. Here, the interfaces are displayed for the small and medium rectangular structures ($h = 0.25$ and $h = 0.5$) at six instants in time between 1.5 and 2.0 s.

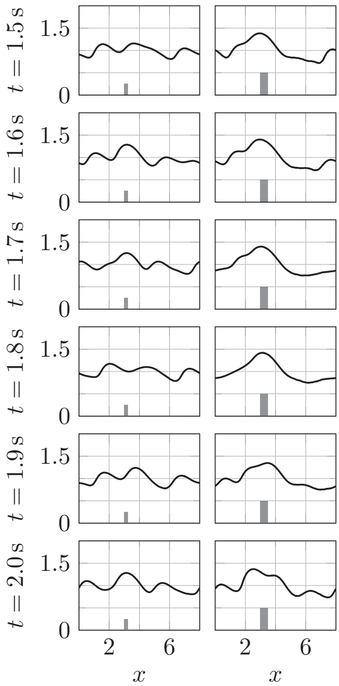

FIG. 7. Shape of the liquid film interface over rectangular microstructures at different instants in time for Re = 70. The domain is compressed and cut off at a height of 2.0. All dimensions are normalized with the respective film thickness δ.

For $h = 0.25$, all films displayed very similar behavior for all Re values (see columns 2 and 5 in Fig. 5). The specific effect of a small triangular compared to a small rectangular microstructure is negligible. At Re < 30 only a slight retention of the film could be observed and no waves, except from the retention of the film, occurred. At Re > 40 this picture suddenly changed and very irregular waves emerged for both structures. Interestingly, the structure of the waves did not really change at even higher Re values (see the second and third columns in Fig. 6).

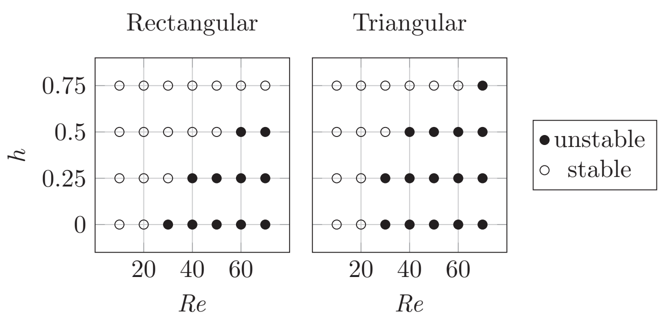

FIG. 8. Instability diagrams for the rectangular (left) and the triangular (right) structures, each for three sizes and seven Reynolds numbers. The results obtained for the smooth plate are added at $h = 0$.

TABLE II. Parameters used in the validation case. δ_{init} represents the initial film height taken from [48].

Case	Re	Ca	A	Cn	Pe_ϵ	δ_{init}
A	16.1	0.063	0.99	0.04	147	0.00244
B	47.95	0.130	0.99	0.04	304	0.00297

C. Discussion

The findings in Figs. 5 and 6 are summarized in the instability diagrams in Fig. 8. Here, we plot the height of the microstructures versus the Reynolds numbers. The stable films are represented as open circles, whereas the unstable films are shown as filled circles. For $h = 0$ we show the results obtained from the smooth plate in both diagrams.

We clearly observe in Fig. 5 that, compared to the film on the smooth plate, all structures shift the formation of waves to higher Re values. This is in accordance with existing studies of rectangular periodic structures (e.g., [7,8,52]). Despite being small compared to the film height, the structures with $h = 0.25$ have a quite extreme effect on the liquid film. They stabilize the film at smaller Re but greatly destabilize the film at larger Re. Furthermore, the inhibiting effect of larger structures compared to smaller structures is visible too. In general, our data indicate that the stabilizing effect, and the inhibition of waves, of the rectangular structures compared to the triangular structures is similar in accordance with [10]. However, we observe a slightly larger inhibition of the rectangular structures. Up to specific values of h and Re rectangular microstructures can prolong the formation of waves to higher Re values compared to the smooth plate (see rectangular, $h = 0.5$, Re < 50) or even completely suppress any waves and instabilities (see rectangular, $h = 0.75$, all Re). An explanation of this stabilizing effect is the greater dissipation in films overflowing sharp corners. In the case of the triangular and rectangular structures the liquid film has to overflow one and two sharp corners, respectively. The dissipated energy is missing from the film to form waves. Furthermore, every structure must be bypassed by the liquid film and recirculation zones are formed before and after the structures. All these factors might be contributing to the stabilization of the liquid film by microstructures with sharp corners.

VI. CONCLUSIONS

In the presented research, we reported on the stability of thin liquid films overflowing single microstructures with sharp corners. The heights of the microstructures were comparable to the film thickness. The dynamics of the two-phase flow were described by the coupling between the Cahn-Hilliard and the Navier-Stokes equations. The selected solution strategy guaranteed efficient and accurate simulations. We validated our implementation against well-known experimental results.

We conducted simulations for Reynolds numbers Re between 10 and 70. The rectangular and triangular microstructures were of heights and widths 0.25, 0.5, and 0.75 compared to the particular Nusselt film thickness. In addition, simulations over a smooth surface were performed for comparison. Our results show some very interesting stabilizing and destabilized effects. Compared to the smooth plate, all structures shift the onset of waves to higher Reynolds numbers. The specific effect of a small triangular compared to a small rectangular microstructure ($h = 0.25$) is negligible. Despite being small compared to the film height, the smaller microstructures greatly destabilized the film at higher Re. Furthermore, the larger the structure compared to the film thickness, the stronger the effect of the inhibition of the formation of waves. Finally, if waves are formed for a critical Re, the waves seem to be much more irregular than in the smooth case. In general, the inhibition of waves is stronger in the rectangular case compared to the triangular structure. In these cases the microstructures act as stabilizers for the liquid film.

Our research indicates a strong influence of the size as well as the geometrical shape of the microstructures on the stability of the liquid film. As known from single-phase flows, one stabilizing

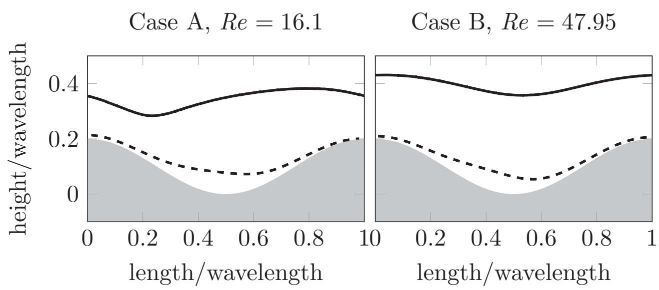

FIG. 9. Liquid film flowing over a deep sinusoidal corrugation, corresponding to the experimental results of Wierschem *et al.* [47] [see Figs. 3(b) and 3(d) therein]. The solid and dashed lines represent the gas-liquid interface and the streamline which separates the recirculation zone from the overflowing film.

effect might be the dissipation of energy in the film while flowing over these sharp corners. Furthermore, the width of the structure might have an impact too. In future research, we will investigate these questions in more detail.

ACKNOWLEDGMENTS

The authors thank Christian Kahle for the fruitful discussions about the Cahn-Hilliard–Navier-Stokes equations. We acknowledge the North-German Supercomputing Alliance (HLRN) for providing HPC resources that contributed to the research results reported in this paper and thank the German Research Foundation (DFG) for the financial support within Project 392533833.

APPENDIX A: VALIDATION VERSUS WIERSCHEM *et al*. [47]

We validated our model and implementation by comparing our results with the experiments reported in [47]. Following the recent work by Dietze [48] as well as the review in [2] the test case used is well established. In the experiments a film of silicone oil overflowed a deep sinusoidal corrugation. The surface was inclined at 8° to the horizontal. Similarly to [48] the Reynolds numbers

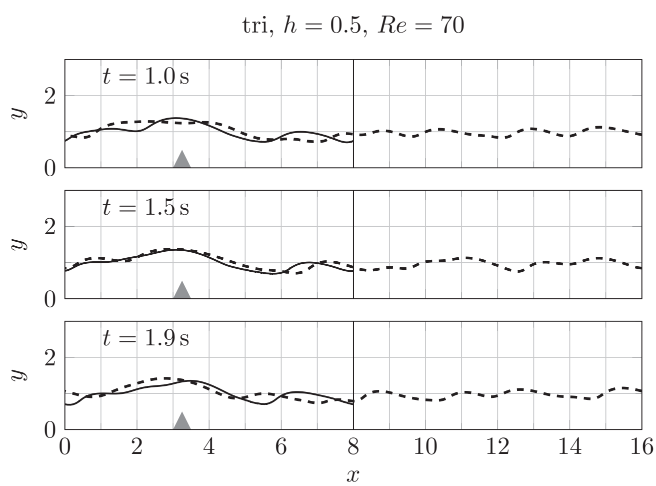

FIG. 10. Comparison of the shape of the liquid film interface over a triangular microstructure for a domain length of $8L$ (solid line) and $16L$ (dashed line). The domain is cut off at a height of $y = 3$. All dimensions are normalized with the respective film thickness δ.

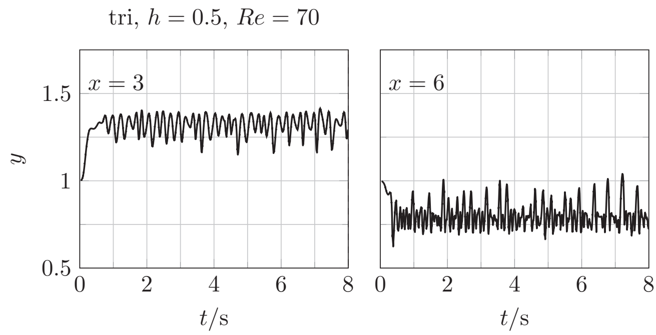

FIG. 11. Height of the liquid film over time for a triangular microstructure at $x = 3$ and $x = 6$. The domain is compressed and cut out at a height between 0.5 and 1.75. All dimensions are normalized with the respective film thickness δ.

Re = 16.1 and Re = 47.95 were simulated. Table II lists the parameters used in the simulations. Our simulation results are shown in Fig. 9. They correspond to the experimental results of Wierschem *et al.* (see Figs. 3(b) and 3(d) in [47]). The solid and dashed lines represent the gas-liquid interface and the streamline which separates the recirculation zone from the overflowing film. Our results are very similar to both the experimental results of Wierschem *et al.* [47] and the numerical results of Dietze [48] (see Fig. 14 therein). The surface shapes of the films including the positions of the minimum are accurately predicted. In the corrugation through separation eddies are formed in sizes similar to those in the experiment and the simulation.

APPENDIX B: VERIFICATION OF DOMAIN LENGTH AND TIME DURATION

We verified our assumption of a periodic domain of length $8L$ by comparing our results to selected simulations with a periodic domain of length $16L$. Exemplarily, we display the results for the triangular microstructure with $h = 0.5$ and Re = 70 in Fig. 10 at different points in time. In the vicinity of the microstructure, we observe only a small difference between the shapes of the liquid films for the different domain lengths. We conclude that in our case $8L$ is sufficient and our assumption of a single microstructure is well represented.

In addition, we verified our assumption that a total time of 2 s already approximates time-periodic results. Exemplarily, we display the height of the film in Fig. 11 at two different positions along the plate over time. Again, we used the triangular microstructure with $h = 0.5$ and Re = 70. It is clearly visible that well before 2 s the film oscillations become almost periodic.

[1] R. V. Craster and O. K. Matar, Dynamics and stability of thin liquid films, Rev. Mod. Phys. **81**, 1131 (2009).

[2] N. Aksel and M. Schörner, Films over topography: From creeping flow to linear stability, theory, and experiments, a review, Acta Mech. **229**, 1453 (2018).

[3] A. Wierschem, M. Scholle, and N. Aksel, Vortices in film flow over strongly undulated bottom profiles at low Reynolds numbers, Phys. Fluids **15**, 426 (2003).

[4] S. J. D. D'Alessio, J. P. Pascal, and H. A. Jasmine, Instability in gravity-driven flow over uneven surfaces, Phys. Fluids **21**, 062105 (2009).

[5] Y. Y. Trifonov, Stability of the wavy film falling down a vertical plate: The DNS computations and Floquet theory, Int. J. Multiphase Flow **61**, 73 (2014).

[6] M. Schörner, D. Reck, and N. Aksel, Stability phenomena far beyond the Nusselt flow - Revealed by experimental asymptotics, Phys. Fluids **28**, 022102 (2016).

[7] K. Argyriadi, M. Vlachogiannis, and V. Bontozoglou, Experimental study of inclined film flow along periodic corrugations: The effect of wall steepness, Phys. Fluids **18**, 012102 (2006).

[8] M. I. Pak and G. H. Hu, Numerical investigations on vortical structures of viscous film flows along periodic rectangular corrugations, Int. J. Multiphase Flow **37**, 369 (2011).

[9] D. Tseluiko, M. G. Blyth, and D. T. Papageorgiou, Stability of film flow over inclined topography based on a long-wave nonlinear model, J. Fluid Mech. **729**, 638 (2013).

[10] M. Schörner, D. Reck, and N. Aksel, Does the topography's specific shape matter in general for the stability of film flows? Phys. Fluids **27**, 042103 (2015).

[11] C. Brunold, J. Hunns, M. Mackley, and J. Thompson, Experimental observations on flow patterns and energy losses for oscillatory flow in ducts containing sharp edges, Chem. Eng. Sci. **44**, 1227 (1989).

[12] M. Ozgoren, Flow structure in the downstream of square and circular cylinders, Flow Meas. Instrum. **17**, 225 (2006).

[13] J. C. Hu, Y. Zhou, and C. Dalton, Effects of the corner radius on the near wake of a square prism, Exp. Fluids **40**, 106 (2006).

[14] M. M. Alam, Y. Zhou, and X. W. Wang, The wake of two side-by-side square cylinders, J. Fluid Mech. **669**, 432 (2011).

[15] S. Veremieiev, H. M. Thompson, and P. H. Gaskell, Free-surface film flow over topography: Full three-dimensional finite element solutions, Comput. Fluids **122**, 66 (2015).

[16] M. G. Blyth and C. Pozrikidis, Film flow down an inclined plane over a three-dimensional obstacle, Phys. Fluids **18**, 052104 (2006).

[17] S. Veremieiev, H. M. Thompson, Y. C. Lee, and P. H. Gaskell, Inertial thin film flow on planar surfaces featuring topography, Comput. Fluids **39**, 431 (2010).

[18] P. H. Gaskell, P. K. Jimack, M. Sellier, H. M. Thompson, and M. C. T. Wilson, Gravity-driven flow of continuous thin liquid films on non-porous substrates with topography, J. Fluid Mech. **509**, 253 (2004).

[19] H. Abels, H. Garcke, and G. Grün, Thermodynamically consistent, frame indifferent diffuse interface models for incompressible two-phase flows with different densities, Math. Models Methods Appl. Sci. **22**, 1150013 (2012).

[20] H. Bonart, C. Kahle, and J.-U. Repke, Comparison of energy stable simulation of moving contact line problems using a thermodynamically consistent Cahn–Hilliard Navier–Stokes model, J. Comput. Phys. **399**, 108959 (2019).

[21] D. Jacqmin, Calculation of two-phase Navier–Stokes flows using phase-field modeling, J. Comput. Phys. **155**, 96 (1999).

[22] M. Wörner, Numerical modeling of multiphase flows in microfluidics and micro process engineering: A review of methods and applications, Microfluid. Nanofluid. **12**, 841 (2012).

[23] D. M. Anderson, G. B. McFadden, and A. A. Wheeler, Diffuse-interface methods in fluid mechanics, Annu. Rev. Fluid Mech. **30**, 139 (1998).

[24] Q. He and N. Kasagi, Phase-field simulation of small capillary-number two-phase flow in a microtube, Fluid Dynam. Res. **40**, 497 (2008).

[25] F. Jamshidi, H. Heimel, M. Hasert, X. Cai, O. Deutschmann, H. Marschall, and M. Wörner, On suitability of phase-field and algebraic volume-of-fluid OpenFOAM® solvers for gas–liquid microfluidic applications, Comput. Phys. Commun. **236**, 72 (2019).

[26] S. Minjeaud, An unconditionally stable uncoupled scheme for a triphasic Cahn-Hilliard/Navier-Stokes model, Numer. Methods Part. Dif. Eqs. **29**, 584 (2013).

[27] G. Grün, F. Guillén-González, and S. Metzger, On fully decoupled, convergent schemes for diffuse interface models for two-phase flow with general mass densities, Commun. Comput. Phys. **19**, 1473 (2016).

[28] J. Shen, X. Yang, and H. Yu, Efficient energy stable numerical schemes for a phase field moving contact line model, J. Comput. Phys. **284**, 617 (2015).

[29] J. H. Ferziger and M. Peric, *Computational Methods for Fluid Dynamics* (Springer, Berlin, 2008), p. 509.

[30] S. Aland, Time integration for diffuse interface models for two-phase flow, J. Comput. Phys. **262**, 58 (2014).

[31] M. Alnæs, J. Blechta, J. Hake, A. Johansson, B. Kehlet, A. Logg, C. Richardson, J. Ring, M. E. Rognes, and G. N. Wells, The FEniCS Project Version 1.5, Arch. Numer. Software **3**, No. 100 (2015).

[32] A. Logg, K.-A. Mardal, and G. Wells (eds.), *Automated Solution of Differential Equations by the Finite Element Method: The FEniCS Book*, Vol. 84 (Springer Science & Business Media, Berlin, 2012).

[33] S. Balay, S. Abhyankar, M. F. Adams, J. Brown, P. Brune, K. Buschelman, L. Dalcin, V. Eijkhout, W. D. Gropp, D. Kaushik, M. G. Knepley, D. A. May, L. C. McInnes, R. T. Mills, T. Munson, K. Rupp, P. Sanan, B. F. Smith, S. Zampini, H. Zhang, and H. Zhang, PETSc website, http://www.mcs.anl.gov/petsc (2018).

[34] S. Balay, S. Abhyankar, M. F. Adams, J. Brown, P. Brune, K. Buschelman, L. Dalcin, V. Eijkhout, W. D. Gropp, D. Kaushik, M. G. Knepley, D. A. May, L. C. McInnes, R. T. Mills, T. Munson, K. Rupp, P. Sanan, B. F. Smith, S. Zampini, H. Zhang, and H. Zhang, Technical Report No. ANL-95/11, *PETSc Users Manual, Revision 3.9*, (Argonne National Laboratory, Lemont, IL, 2018).

[35] S. Balay, W. D. Gropp, L. C. McInnes, and B. F. Smith, Efficient management of parallelism in object oriented numerical software libraries, in *Modern Software Tools in Scientific Computing*, edited by E. Arge, A. M. Bruaset, and H. P. Langtangen (Birkhäuser Press, Boston, MA, 1997), pp. 163–202.

[36] P. R. Amestoy, I. S. Duff, J. Koster, and J.-Y. L'Excellent, A fully asynchronous multifrontal solver using distributed dynamic scheduling, SIAM J. Matrix Anal. Appl. **23**, 15 (2001).

[37] P. R. Amestoy, A. Guermouche, J.-Y. L'Excellent, and S. Pralet, Hybrid scheduling for the parallel solution of linear systems, Parallel Comput. **32**, 136 (2006).

[38] P. Boyanova, D.-Q. Minh, and M. Neytcheva, Efficient preconditioners for large scale Binary Cahn-Hilliard models, Comput. Methods Appl. Math. **12**, 1 (2012).

[39] J. Bosch, C. Kahle, and M. Stoll, Preconditioning of a coupled Cahn-Hilliard Navier-Stokes system, Commun. Comput. Phys. **23**, 603 (2018).

[40] J. Blechta, Towards efficient numerical computation of flows of non-Newtonian fluids, Ph.D. thesis, Charles University, Faculty of Mathematics and Physics, 2019, https://hdl.handle.net/20.500.11956/108384.

[41] M. A. Olshanskii and Y. V. Vassilevski, Pressure Schur complement preconditioners for the discrete Oseen problem, SIAM J. Sci. Comput. **29**, 2686 (2007).

[42] H. Elman, V. E. Howle, J. Shadid, R. Shuttleworth, and R. Tuminaro, A taxonomy and comparison of parallel block multi-level preconditioners for the incompressible Navier-Stokes equations, J. Comput. Phys. **227**, 1790 (2008).

[43] N. Bootland, A. Bentley, C. Kees, and A. Wathen, Preconditioners for two-phase incompressible Navier-Stokes flow, SIAM J. Sci. Comput. **41**, B843 (2019).

[44] S. Hysing, S. Turek, D. Kuzmin, N. Parolini, E. Burman, S. Ganesan, and L. Tobiska, Quantitative benchmark computations of two-dimensional bubble dynamics, Int. J. Numer. Methods Fluids **60**, 1259 (2009).

[45] H. Bonart, J. Jung, C. Kahle, and J.-U. Repke, Influence of liquid density and surface tension on the pinning of sliding droplets on a triangular microstructure, Chem. Eng. Technol. **42**, 1381 (2019).

[46] H. Bonart and J.-U. Repke, Direct numerical simulations of liquids on microstructured surfaces: Analysing the fluid dynamics on packing, Chem. Eng. Trans. **69**, 61 (2018).

[47] A. Wierschem, T. Pollak, C. Heining, and N. Aksel, Suppression of eddies in films over topography, Phys. Fluids **22**, 113603 (2010).

[48] G. F. Dietze, Effect of wall corrugations on scalar transfer to a wavy falling liquid film, J. Fluid Mech. **859**, 1098 (2019).

[49] C. Geuzaine and J.-F. Remacle, Gmsh: A 3-D finite element mesh generator with built-in pre- and post-processing facilities, Int. J. Numer. Methods Eng. **79**, 1309 (2009).

[50] X. Cai, H. Marschall, M. Wörner, and O. Deutschmann, Numerical simulation of wetting phenomena with a phase-field method using OpenFOAM®, Chem. Eng. Technol. **38**, 1985 (2015).

[51] S. J. Baxter, H. Power, K. A. Cliffe, and S. Hibberd, Three-dimensional thin film flow over and around an obstacle on an inclined plane, Phys. Fluids **21**, 032102 (2009).

[52] M. Vlachogiannis and V. Bontozoglou, Experiments on laminar film flow along a periodic wall, J. Fluid Mech. **457**, 133 (2002).